EES Batteries

PAPER

View Article Online
View Journal | View Issue

Cite this: *EES Batteries*, 2025, **1**, 1720

Electrochemo-mechanical effects of Co-free layered cathode on interfacial stability in all-solid-state batteries under high-voltage operation

Jinhee Jung,†[a,c] Joonhyeok Park,†[b] Jun Lim,[a] Jinwoo Jeong,[a] Yeseung Lee,[a] Jaeik Kim,[b] Seungwoo Lee,[b] Byungjin Choi,[c] Seong Ji Ye,[c] Jong Sung Jin,[d] Ji Yeong Sung,[d] Ungyu Paik *[b] and Taeseup Song *[a,b]

Ni-rich layered oxide cathode active materials (CAMs), such as $LiNi_xCo_yMn_zO_2$ (NCM), are promising candidates for high-energy all-solid-state batteries (ASSBs) due to their high theoretical capacities. However, Ni-rich NCMs suffer from poor electrochemical performance and mechanical degradation caused by anisotropic volume changes during high-voltage cycling. Cobalt in NCM further promotes irreversible lattice oxygen redox and phase transitions, leading to mechanical and interfacial degradation under high-voltage conditions. In this study, we introduce a Co-free layered oxide ($LiNi_{0.75}Mn_{0.25}O_2$, NMX75) to improve cycling stability under high-voltage operation in sulfide-based ASSBs. A comparative study between NMX75 and NCMs demonstrated that NMX75 effectively mitigates chemo-mechanical degradation by suppressing volume changes and mechanical stress. On the particle level, the NMX75 mitigated internal void formation and enabled structurally stable Li^+ intercalation/deintercalation. On the interface level, the mitigation of mechanical degradation suppressed solid electrolyte decomposition and enhanced interfacial stability. As a result, the NMX75 delivered 80.6% capacity retention after 100 cycles at 2.5–4.45 V (*vs.* Li/Li^+) in sulfide-based ASSBs. The outstanding performance of NMX75 provides fundamental insights into the development of the next-generation ASSBs.

Received 24th July 2025,
Accepted 2nd September 2025

DOI: 10.1039/d5eb00136f

rsc.li/EESBatteries

Broader context

The accelerating demand for electric vehicles and energy storage systems has intensified the need for all-solid-state batteries (ASSBs) with high energy density and long-term cycling stability. Ni-rich layered oxide cathodes such as $LiNi_xCo_yMn_zO_2$ (NCM) offer high theoretical capacities but suffer from rapid mechanical and interfacial degradation under high-voltage operation, largely due to anisotropic volume changes and irreversible phase transitions. In particular, cobalt in NCM contributes to lattice oxygen redox activity, which promotes structural instability and side reactions with sulfide-based solid electrolytes. These challenges hinder the commercialization of high-energy ASSBs. In this work, we introduce a Co-free layered oxide ($LiNi_{0.75}Mn_{0.25}O_2$, NMX75) that addresses these limitations by suppressing chemo-mechanical degradation and enhancing interfacial stability. The absence of cobalt minimizes oxygen redox and structural collapse, while the Mn substitution helps to maintain the structural integrity during cycling. This strategy enables stable high-voltage cycling with reduced pressure variation, paving the way for safer and more durable ASSBs. Our findings highlight the importance of compositional engineering in cathode materials and provide design insights for next-generation sustainable energy storage technologies.

Introduction

The global community, including the European Union (EU), the United States, and China, has been actively working to reduce greenhouse gas emissions to achieve net-zero targets by 2050.[1] These efforts are closely linked to the Sustainable Development Goals (SDGs).[2] Rechargeable batteries, particularly lithium-ion batteries (LIBs), play a crucial role in reducing the carbon footprint, especially through their application in electric vehicles (EVs) and large-scale energy storage systems

[a]*Department of Battery Engineering, Hanyang University, 222 Wangsimni-ro, Seoul, 04763, Republic of Korea*
[b]*Department of Energy Engineering, Hanyang University, 222 Wangsimni-ro, Seoul, 04763, Republic of Korea. E-mail: upaik@hanyang.ac.kr, tssong@hanyang.ac.kr*
[c]*LG Chem, Ltd, Cathode Materials R&D Center, 188 Munji-ro, Daejeon, 34122, Republic of Korea*
[d]*Busan Center, Korea Basic Science Institute (KBSI), 30 Gwahaksandan 1-ro 60beon-gil, Busan, 46742, Republic of Korea*
†These authors contributed equally to this work.

(ESS).[3] As the LIBs market continues to grow rapidly, advancements in battery technology are becoming increasingly important.[4]

LIBs offer high energy density, but because they use organic liquid electrolytes, they have safety issues such as thermal runaway.[5] All-solid-state batteries (ASSBs) based on solid electrolytes (SEs) are regarded as one of the most promising next-generation battery technologies due to their higher energy density and improved safety.[6,7] Among the SEs, sulfide-based solid electrolytes have attracted much attention due to their high ionic conductivity (>1 mS cm^{-1} at 298 K), and malleable property.[8–10] The use of cathode active materials (CAMs) in ASSBs with high operating voltage and capacity is expected to enhance the energy density of batteries.[11,12] Layered oxide cathode materials, $LiNi_xCo_yMn_zO_2$ (NCM), which have been extensively investigated as CAMs for advanced LIBs, are also strong candidates for integration into practical ASSBs at scale.[13,14]

In general, there are two strategies for high energy density of NCM in LIBs: (1) One approach is increasing the proportion of redox-active Ni (≥80%, Ni-rich NCM) in NCM to enhance the specific capacity.[15–17] (2) The other is raising the cut-off voltage, which can be achieved using medium Ni content in NCM.[18,19] However, the electrochemical performances of NCM for high energy density in ASSBs are still far behind expectation especially compared to LiBs.[20,21] The poor electrochemical performance of Ni-rich NCMs in ASSBs is primarily due to interfacial instability.[22–24] Electrochemo-mechanical effects and inter-diffusion between oxygen and sulfur species occur at the interface between the CAM and the SE in ASSBs.[25–27] The anisotropic volume changes of NCM operating at high-voltage induces a stress at the interface between NCM and SEs, resulting in physical degradation such as crack formation.[28,29] The crack formation results from volume changes during cycling, which can cause a contact loss between Ni-rich NCM and SEs.[24,30,31] It has also been shown that structural transformation occurs within the CAMs, which induces additional stresses that cause cracking, especially for high-Ni NCM at high voltages.[32] To address the contact loss problem between NCMs and SEs, single-crystalline (SC) NCMs have been extensively investigated.[33] Conventional Polycrystalline (PC)-NCMs suffer from microcrack nucleation and propagation caused by anisotropic volume changes between primary particles and internal stress at grain boundaries due to repeated Li ion extraction/insertion during cycling.[34,35] This results in poor electrical contact with the SE, reduced capacity, and eventually the poor electrochemical performance. SC-NCMs improve structural strength by eliminating the grain boundary cracking problem that occurs in conventional PC-NCMs.[36,37] It has the advantage of inducing more uniform volume changes than PC-NCMs to increase cycle stability.[38] However, research has shown that SC-NCMs still undergo overall volume changes during Li ion extraction/insertion at operating high-voltage and do not show isotropic volume changes because of the facet crystallographic orientation and the anisotropic changes in the *a* and *c*-axis.[32,39] Therefore, SC-NCMs may not be the ideal solution for fully solving the chemical-mechanical problems.[40] More research and improvements are needed to solve the problem of interfacial contact between NCMs and SEs at high voltage. Cobalt is crucial for preserving the structural stability of NCMs during the initial cycle.[41,42] However, at high voltage, it is known to trigger lattice oxygen release leading to irreversible phase transitions that degrade the structural integrity of NCMs.[43,44] In addition, previous studies have shown that Co-containing layered oxides such as LCO and NCM suffer from severe interfacial degradation when in contact with sulfide electrolytes, forming resistive interphases including Li_3PO_4 and transition-metal sulfides.[45,46] Thus, it is necessary to study the Co-free layered structural CAMs in ASSBs. Co-free, Ni-rich Layered NMX materials provide an effective way to reduce costs caused by Co while maintaining the content of Ni, which increases electrochemical property, and increasing the content of Mn, which is beneficial to cycling stability and thermal stability at high voltage.[41,47]

In this work, we report a single-crystalline Co-free layered oxide cathode material, $LiNi_{0.75}Mn_{0.25}O_2$ (NMX75), with high voltage stability in sulfide-based ASSBs. We focused on the electrochemo-mechanical effect to understand the performance degradation of ASSBs. This effect describes how volume changes during Li ion insertion and extraction cause loss of interfacial contact and degradation of electrochemical performance. The electrochemo-mechanical effect of Co-free layered cathode materials plays a crucial role in ASSBs. To investigate this, we conducted a comparative study between $LiNi_{0.60}Co_{0.20}Mn_{0.20}O_2$ (NCM60) and Co-free NMX75. The Ni : Mn ratio was fixed at 3 : 1 in both samples, thereby minimizing the influence of Mn and allowing the performance difference to be attributed to the presence of Co.[48,49] We evaluated the electrochemical performance at a high cut-off voltage (2.5–4.45 V, *vs.* Li/Li^+). Furthermore, Electrochemical Impedance Spectroscopy (EIS) and Distribution of Relaxation Times (DRT) were employed to investigate the mechanical and chemical degradation mechanisms that contribute to the improved electrochemical performance of Co-free NMX75 compared to NCM60.[50] Combined analysis using *ex situ* X-Ray diffraction (XRD) and digital electric press showed that Co-Free NMX75 has better mechanical stability than NCM60 during high voltage cycling. In addition, we investigated the interface between CAMs and SEs, using scanning transmission electron microscopy (STEM), Energy-Dispersive Spectroscopy (EDS) techniques, X-ray photoelectron spectroscopy (XPS) and Time-of-Flight Secondary Ion Mass Spectrometry (ToF-SIMS). We also compared the Co-free NMX75 with a Ni-rich NCM ($LiNi_{0.80}Co_{0.10}Mn_{0.10}O_2$, NCM80), emphasizing how Co-free layered cathodes can address interfacial and mechanical challenges and contribute to the commericialization of high-energy-density ASSBs.

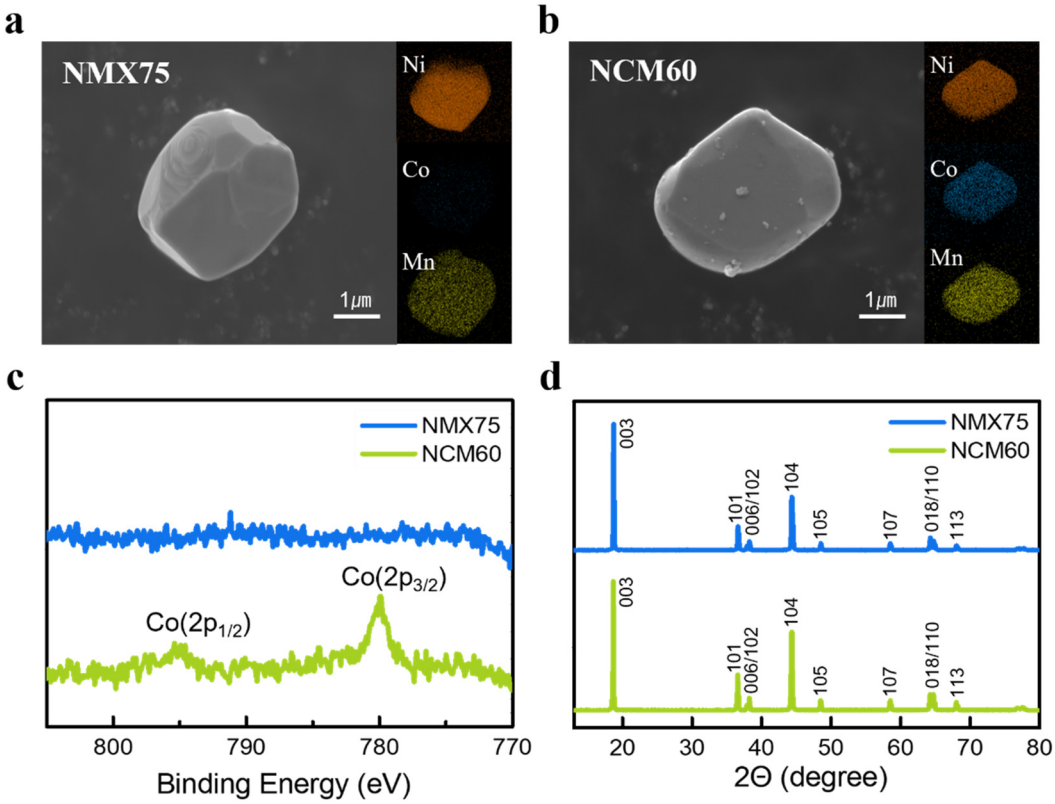

Fig. 1 (a and b) SEM images and EDS elemental maps of NMX75 and NCM60. (c) XPS spectra showing the Co $2p_{1/2}$ and $2p_{3/2}$ peaks of NMX75 and NCM60. (d) XRD patterns of NMX75 and NCM60.

Results and discussion

Fig. 1 compares the characterization of NMX75 and NCM60 cathode active materials (CAMs) with different Co compositions. Fig. 1a and b show scanning electron microscopy (SEM) images and energy dispersive X-ray spectroscopy (EDS) mappings of NMX75 and NCM60, respectively. NMX75 and NCM60 have a single-crystalline morphology and particle size of 3–4 μm (Fig. S1 and Table S1). Since the particle size of the CAM plays a critical role in the performance of all-solid-state batteries, CAMs with comparable sizes were selected to eliminate particle size effects.[51] In addition, surface modification was not observed on the CAM particles in the SEM images. EDS mapping results confirm the presence of Co signal in NCM60, whereas no Co signal is observed in NMX75. Consistently, XPS analysis reveals the absence of the Co $2p_{1/2}$ and Co $2p_3/_2$ peaks in NMX75, further verifying its Co-free composition (Fig. 1c). Inductively coupled plasma optical emission spectroscopy (ICP-OES) further confirmed the absence of Co in NMX75 (Table S2).[52]

X-ray diffraction (XRD) patterns of NMX75 and NCM60, shown in Fig. 1d, indicate that both samples have a well-defined α-$NaFeO_2$ structure (space group $R\bar{3}m$).[11] The splitting between the (006)/(102) and (018)/(110) peaks indicates that both samples have a well-ordered layered structure.[40]

Full-cells employing lithium metal anode and Li_6PS_5Cl (LPSC) SE layer were fabricated to evaluate the electrochemical performance of NMX75 and NCM60 composite cathodes using a pressed cell. Fig. 2a shows the initial charge–discharge profiles of full-cells employing NMX75 and NCM60 composite cathodes in the high-voltage range of 2.5–4.45 V at 0.1C rate and room temperature. The NMX75 and NCM60 composite cathodes showed specific discharge capacities of 184.4 mAh g^{-1} and 159.7 mAh g^{-1}, respectively. Their initial coulombic efficiencies were 82.3% and 75.0%. Notably, under this high-voltage operation, the NMX75 composite cathode exhibited improved discharge capacity and coulombic efficiency compared to NCM60 composite cathode, which was not observed under a voltage window of 2.5–4.25 V (Fig. S2). This enhancement in the electrochemical performance of NMX75 composite cathode is attributed to a reduced interfacial resistance between CAMs and SEs.[53] The rate capabilities of full-cells employing NMX75 and NCM60 composite cathode were evaluated at various current rates (Fig. 2b). The full-cell employing NMX75 composite cathode delivered average discharge capacities of 175.5, 160.3, 146.8, 118.1, and 58.7 mAh g^{-1} at 0.1, 0.2, 0.5, 1, and 2C, respectively. In contrast, the full-cell employing NCM60 composite cathode exhibited average discharge capacities of 146.1, 129.1, 113.0, 83.2, and 30.4 mAh g^{-1} at the same C-rates. These results suggest that the interfacial resistance between CAMs and SE plays a critical role.[54]

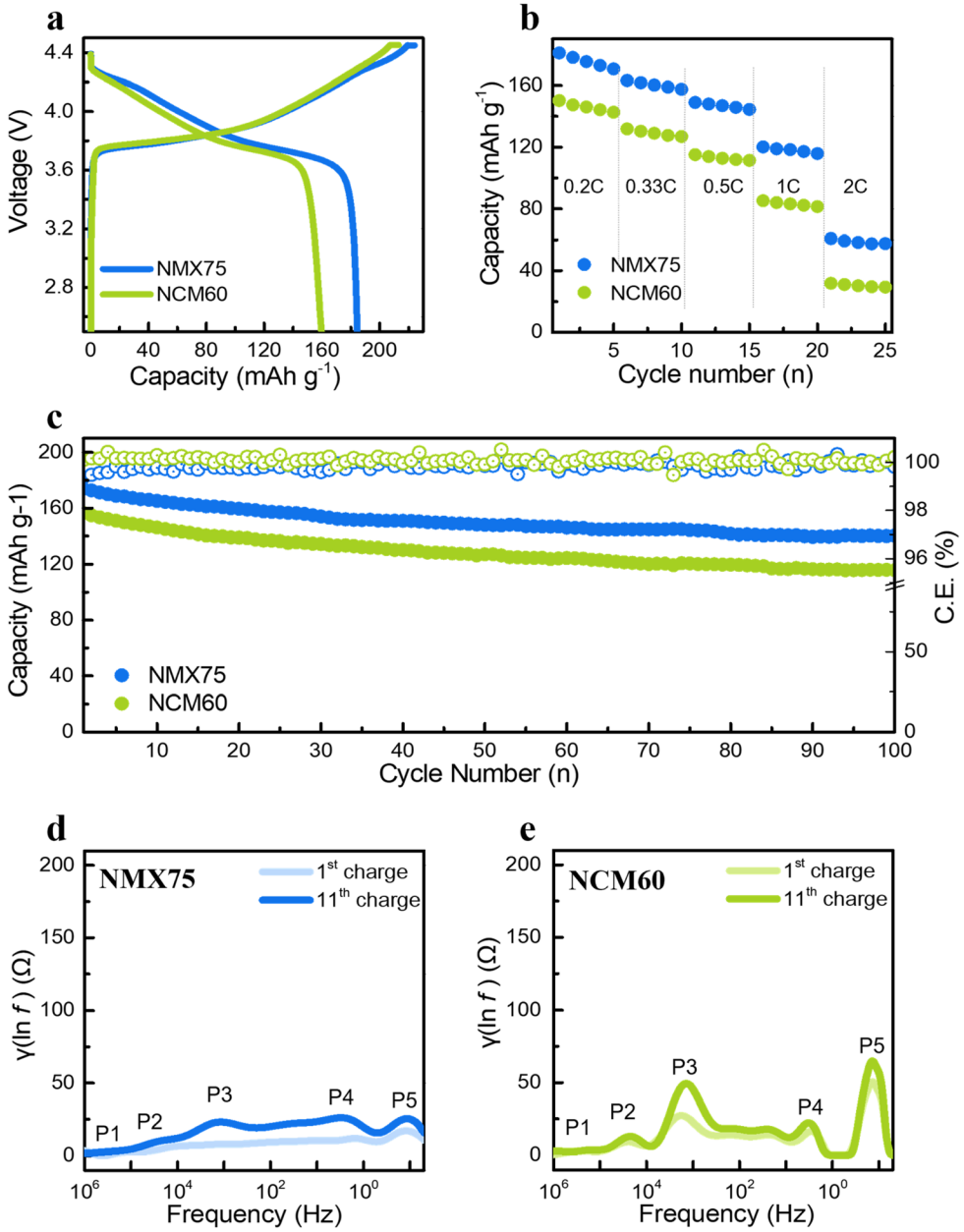

Fig. 2 (a) Initial charge–discharge curves at 0.1C. (b) Rate capabilities. (c) Cycling performance over 100 cycles at 0.2C. (d) DRT profiles after 10 cycles for NMX75. (e) DRT profiles after 10 cycles for NCM60.

Fig. 2c displays the cycling stability of the full-cell employing NMX75 and NCM60 composite cathode. The capacity retention of the ASSBs employing NMX75 composite cathode and NCM60 composite cathode was 80.6% and 73.9%, respectively, after 100 cycles. Compared to the cycling stability in the voltage range of 2.5–4.25 V (Fig. S3), the NMX75 composite cathode maintained capacity retention, whereas the NCM60 composite cathode exhibited a significant capacity fade. The higher-Ni-content NMX75 composite cathode exhibited better high-voltage cycling performance than the NCM60 composite cathode. These results demonstrate that NMX75 provides superior cycling stability compared to NCM60 in sulfide-based SE under high-voltage operation. To investigate the interface resistance between CAM and SE, electrochemical impedance spectroscopy (EIS) was measured with the studies before and after cycling. Fig. S4 and S5 exhibit the EIS results for full-cells employing NMX75 and NCM60 composite cathodes, respectively, measured before and after cycling in the voltage range of 2.5–4.45 V. The bulk resistance (R_b) of the SE is represented by x-axis intercept at high frequencies, while the grain boundary charge transfer resistance (R_{gb}) is indicated by the semicircle in the mid-frequency range.[55] In the low-frequency region, the semicircle reflects the interfacial resistance (R_{int}).[56,57] The sum of R_{gb} and R_{int} gives the total internal resistance (R_t).[58] As

shown by the R_t values, the NMX75 composite cathode exhibits negligible change in total internal resistance before and after cycling, whereas the NCM60 composite cathode shows a noticeable increase in resistance after cycling. The distribution of relaxation times (DRT) analysis was conducted on the EIS spectra to obtain a more detailed understanding of the resistive responses.[59] This approach allows for the deconvolution of overlapping electrochemical processes, providing distinct separation of individual impedance contributions.[60] Fig. 2d and e present the DRT profiles, measured after 1 and 10 cycles, respectively. Five major peaks, labeled P1 to P5 in order of decreasing frequency, are observed in the corresponding DRT profiles. The high-frequency peak (P1) is attributed the grain boundary resistance of SE (R_{SE}), whereas the medium-frequency components (P2, P3, and P4) are associated with the resistance of the solid electrolyte interphase (R_{SEI}), the mechanical contact impedance between the active material and solid electrolyte, and the charge transfer resistance (R_{ct}), respectively.[61] The distribution in the low-frequency region (P5) corresponds to the resistance associated with lithium-ion diffusion ($W_{diffusion}$).[62,63] The NMX75 composite cathode shows a smaller increase in mechanical impedance (P3) after 10 cycles. In contrast, the NCM60 composite cathode shows a significant increase in mechanical contact impedance (P3) after 10 cycles. Mechanical impedance (P3) observed in the NCM60 composite cathode after 10 cycles is mainly attributed to the cathode, indicating a mechanical contact issue at the interface between CAM and SE.[62] The presence of voids at the interface between the CAM and SE can induce heterogeneous electrochemical reactions at the interface, leading to localized stress and progressive degradation of interfacial contact during cycling. In contrast, the NMX75 cell shows a smaller increase in impedance, suggesting improved interfacial compatibility between CAMs and SEs.

To investigate the mechanism behind the outstanding electrochemical performance under high-voltage operation of NMX75 in sulfide-based ASSBs, an analysis was conducted focusing on two levels: (1) particle level, (2) interface level.

The investigation focused on the particle level, analyzing the void formation of NMX75 and NCM60 composite cathode. Cross-section SEM images of the NMX75 and NCM60 composite cathode interface between CAMs and SE were obtained after 10 cycles (Fig. 3a and b). The NMX75 and NCM60 composite cathodes exhibited stable interfaces between CAMs and SEs without void formation before cycling (Fig. S6). Cross-sectional SEM images after 10 cycles show that void formation was observed at the CAM/SE interface in NCM60, whereas no void formation was observed in NMX75. The volume changes induced by repeated lithiation and delithiation can increase interfacial stress between the CAMs and SEs, while the formation of voids can elevate the Li ion pathways, thereby increasing interfacial impedance. To investigate in-*operando* electrode volume changes related to interfacial contact issues, a digital electric press was used to apply and maintain a constant uniaxial stack pressure in ASSBs (Fig. 3c). Fig. S7 shows the schematic illustration of the digital electric press in the ASSBs. $Li_4Ti_5O_{12}$ (LTO), which is known to exhibit negligible volume changes during cycles, was employed as an anode electrode.[64] This allowed the effects of cathode volume changes on charge–discharge capacities to be isolated and analyzed. The measured pressure change for the NMX75 composite cathode is smaller than that for the NCM60 composite cathode under 100 MPa. Although NMX75 composite cathode exhibited a higher specific discharge capacity than NCM60 composite

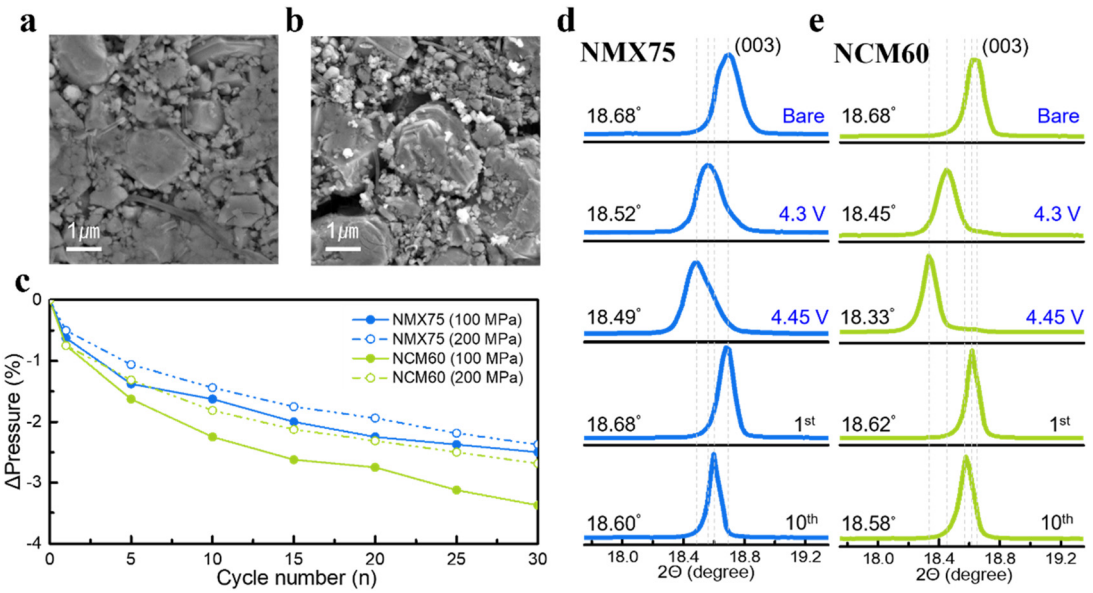

Fig. 3 (a and b) FIB–SEM images of NMX75 and NCM60 composite cathodes after 10 cycles at a high cut-off voltage of 4.45 V, respectively. (c) Volume changes behavior of full cells during cycling, measured using a digital electric press under constant pressure. (d and e) *Ex situ* XRD analysis showing the electrochemo-mechanical evolution of the composite cathodes at different voltage stages: (d) NMX75 and (e) NCM60.

cathode, it showed less volume changes (Fig. S8). Similarly, under a higher pressure of 200 MPa during cycling, the pressure change measured for the NMX75 composite cathode remained smaller than that for the NCM60 composite cathode, despite its higher discharge capacity (Fig. S9). As the applied pressure increased, the extent of volume change in both NMX75 and NCM60 composite cathodes decreased, which is attributed to the suppression of void formation at the interface between CAMs and SEs under elevated pressure. This result, as shown in the cross-sectional SEM image, indicates that NMX75 particles exhibit less interfacial void formation compared to NCM60 particles.

Ex situ XRD was employed to determine the degree of lithiation in NMX75 and NCM60 composite cathode by monitoring peak shifts during cycling under high-voltage operation (Fig. S10). Fig. 3d and e show the XRD (003) peak shifts of NMX75 and NCM60 composite cathode. In the initial cycles, the (003) peaks were observed at 18.68° indicate no significant difference between NMX75 and NCM60 particles. However, during repeated cycling, the (003) peak of NCM60 particles gradually shifted to the left, which is attributed to the degradation of interparticle contact and increasingly incomplete Li insertion/extraction. In contrast, NMX75 particles exhibited a smaller peak shift while achieving a higher specific discharge capacity, indicating less interfacial degradation caused by volumetric changes. A comparative analysis of lattice collapse at the same cut-off voltage reveals that, although NMX75 particles undergoes substantially higher Li extraction than NCM60 particles, its structural changes are significantly less pronounced. These results indicate that the lattice stability of NMX75 particles is intrinsically superior under high-voltage operation.

The decomposition of the CAM/SE and interphase formation at the interface of the NMX75 and NCM60 composite cathodes were analyzed. Fig. 4a and b show atomic-scale high-angle annular dark-field scanning TEM (HAADF-STEM) images of NMX75 and NCM60. High-resolution TEM (HR-TEM) specimens were prepared using the focused ion beam (FIB) technique (Fig. S11). The NCM60 composite cathode showed intragranular cracking after 10 cycles. The layered structures of both NMX75 and NCM60 were further confirmed through HR-TEM (Fig. S12) and fast Fourier transform (FFT) images (Fig. S13). In both samples, the HAADF-STEM images exhibit a bright contrast at the interface between CAMs and SEs, attributed to the interdiffusion of transition metal and O–S element after cycling. The bright region observed in the HAADF-STEM images is ascribed to the interdiffusion of oxygen and sulfur.[65] This interdiffusion at the CAM/SE interfaces was confirmed in both NMX75 and NCM60 when employing uncoated layered cathodes. To investigate the effect of cobalt presence on the degree of interdiffusion, energy dispersive spectroscopy (EDS) analysis of NMX75 and NCM60 was conducted (Fig. S14 and S15). The EDS line profiles of NMX75 and NCM60 were obtained across the interfaces between CAMs and SEs (Fig. S16). The EDS line profiles marked by the green boxes in Fig. 4a and b. Diffused transition metal elements, particularly Ni, were found to be distributed from the surface of both NMX75 and NCM60. Notably, elemental interdiffusion was also observed in the Co-free NMX75, indicating that cobalt is not solely responsible for suppressing interdiffusion. These results indicate that the reduced interfacial resistance observed in NMX75, relative to NCM60, is not attributed to the interdiffusion of transition metals and O–S elements but is instead governed by the intrinsic electrochemo-mechanical properties of the CAM.[46] The enhanced mechanical stability of the Co-free layered NMX75 is attributed to its intrinsic structural characteristics.[43] In conventional layered NCMs, cobalt promotes excessive lattice oxygen activation under high-voltage conditions, leading to oxygen release, irreversible phase transitions, and mechanical degradation such as intragranular cracking.[66] The absense of cobalt suppresses lattice oxygen redox reactions during deep delithiation under high-voltage condition, thereby preventing irreversible phase transitions and preserving the layered structure. Co-free layered NMX75 effectively mitigated volume change, interfacial void formation, and mechanical degradation during high-voltage cycling in sulfide-based ASSBs. It is evident that the electrochemo-mechanical effect dominates the difference in the electrochemical performances of ASSBs employing NMX75 and NCM60.

Fig. 4c and d show that the detailed signals of S 2p and P 2p change in NMX75 and NCM60 composite cathodes before and after cycling. The SI also contains the O 1s signal (Fig. S17). Prior to analysis, all XPS spectra were calibrated against the C 1s peak at 284.8 eV. The S 2p and P 2p signals are split into two peaks due to spin–orbit coupling, exhibiting an area ratio of approximately 2 : 1. Each distinct chemical environment of sulfur or phosphorus gives rise to a characteristic $2p_{3/2}$–$2p_{1/2}$ doublet.[45]

Before cycling, the main S 2p peak of NMX75 and NCM60 composite cathodes appear at 161.6 eV ($2p_{3/2}$), corresponding to sulfide species derived from the sulfide-based SE and composite cathodes. The blue peak near 159.9 eV is attributed to S^{2-} in LPSC, while the peak around 164.4 eV corresponds to S^0 species such as polysulfides. Green peaks indicate P–S bonds in PS_4^{3-} tetrahedra, orange peaks arise from bridged P–S–P units in $P_2S_7^{4-}$, and red peaks reflect more oxidized sulfur and phosphorus species.[67] The red peaks in the P 2p and S 2p spectra were not observed both NMX75 and NCM60 composite cathodes before cycling. The formation of –S–S– linkages and oxidized phosphorus species ($P–O_x$) indicates the development of LPSC decomposition at the interface between CAMs and SEs. After cycling, NMX75 composite cathodes exhibits less decomposition of LPSC compared to NCM60 composite cathodes. The greater amount of LPSC decomposition in the NCM60 composite cathodes compared to the NMX75 composite cathodes is attributed to the following factor. In the NCM60 composite cathode, a higher amount of LPSC decomposition is generated by interfacial contact loss and cracking of CAMs, which increases the interfacial resistance between CAMs and SEs.

Fig. 4e and f show time-of-flight secondary ion mass spectrometry (ToF-SIMS) analysis used to evaluate the relative con-

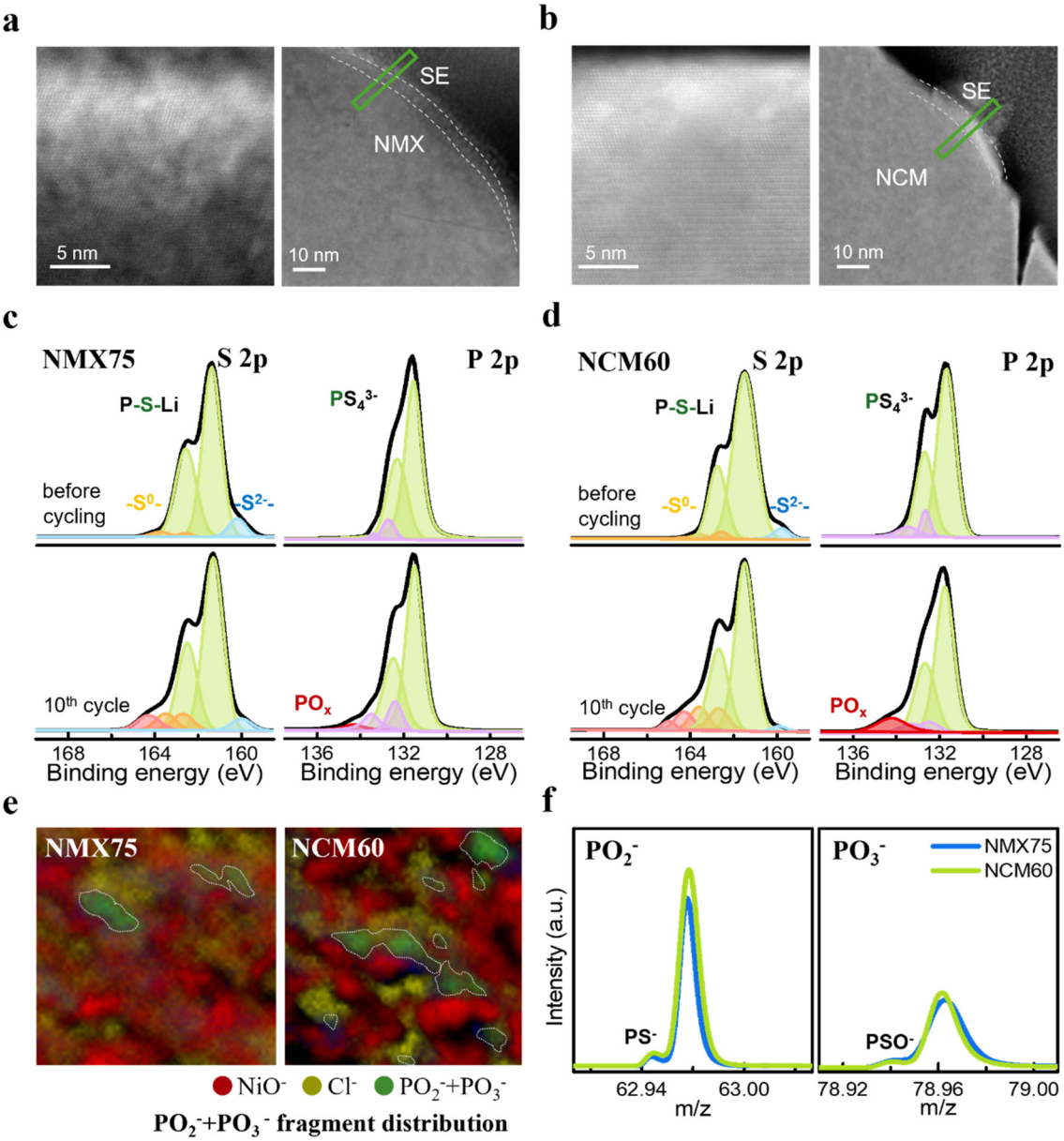

Fig. 4 (a and b) STEM images of the surface layers of NMX75 and NCM60 composite cathodes after 10 cycles at a high cut-off voltage of 4.45 V. (c and d) XPS Spectra of S 2p and P 2p regions for NMX75 and NCM60, respectively, before and after 10 cycles. (e) ToF-SIMS chemical species mapping images showing the distribution of NiO^- (red), Cl^- (yellow), and PO_x^- (green) after 10 cycles. (f) Mass spectra of PO_x^- fragments.

centrations of LPSC decomposition products. ToF-SIMS enables high-sensitivity detection of the spatial distribution and chemical evolution, allowing the detection of trace levels of LPSC decomposition in the composite cathodes. ToF-SIMS depth profiling experiments were performed in the near-surface region to investigate the local distributions of phosphate (PO_x^-) fragments.[46] Note that the intensities were normalized to the total ion intensity. Fig. 4e presents the surface distribution of the ToF-SIMS chemical species in NMX75 and NCM60 composite cathodes after 10 cycles, indicating the localization of PO_x^- fragments. The red, yellow, and green signals correspond to NiO^-, Cl^-, and PO_x^- fragments, respectively. For an accurate quantitative comparison of PO_x^- between NCM60 and NMX75, a total count comparison was conducted (Table S3). A higher intensity of PO_x^- fragments was observed in NCM60 composite cathodes compared to NMX75 composite cathodes, which corresponds to the signal intensity of PO_x^- fragments shown in Fig. 4f. Furthermore, NCM60 composite cathode exhibited black regions lacking Cl^- from the SEs and NiO^- from the CAMs compared to NMX75 composite cathodes, indicating the formation of interfacial voids (Fig. S18). The presence of PO_x^- species serves as an indicator of increased interfacial resistance due to the LPSC decomposition at the interface between CAMs and SEs. The electrochemo-mechani-

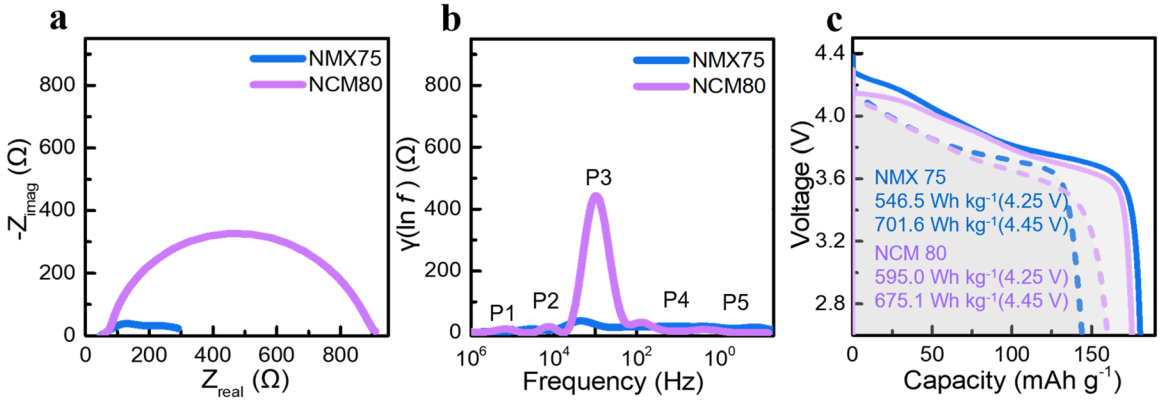

Fig. 5 (a) Nyquist plots after 30 cycles of NMX75 and NCM80 in the voltage range of 2.5–4.45 V. (b) Corresponding DRT result. (c) Calculated energy densities of NMX75 and NCM80, based on initial capacity at each cut-off voltage.

cal effect of NMX75 enabled more stable physical contact at the CAM/SE interface, which likely contributed to improved interfacial integrity during cycling.

Fig. S19 shows the SEM images and EDS mapping results of conventional single-crystalline Ni-rich NCM80. Similar to NMX75, NCM80 exhibits a particle size of 3–4 μm (Fig. S20). Fig. S21 shows the initial charge–discharge curves at 0.1C and cycling performance at 0.2C of the NCM80 composite cathode within the voltage range of 2.5–4.45 V. The discharge capacity of NCM80 composite cathode was 191.7 mAh g^{-1} with initial coulombic efficiency of 83.2%. This difference is attributed to the higher Ni content in NCM80, which contributes more to the redox reactions compared to NMX75. The cycling performance of the cells at a current density of 0.1C was also evaluated. Unlike the cell cycled within the voltage range 2.5 and 4.25 V (Fig. S22), the full-cell employing NCM80 experienced a short circuit after 52 cycles under high-voltage operation. The EIS and DRT analyses of each sample after 30 cycles are shown (Fig. 5a and b). The EIS and DRT results reveal that the high volume changes of NCM80 served as a major cause of interfacial degradation. In contrast, stable cycling performance was achieved by maintaining interfacial integrity through suppression of void formation at the CAM/SE interface. In Ni-rich layered CAMs, it is well known that the *c*-axis of the crystal structure initially expands upon Li ion extraction during charging, followed by a sudden contraction associated with the H2–H3 phase transition. The initial expansion occurs because the extraction of Li ions increases the repulsive force between the Li–O layers. Once a certain amount of Li is removed, the distance between oxygen layers decreases, and van der Waals interactions lead to a contraction of the *c*-axis. During discharge, reinsertion of Li ion causes the lattice to expand again.[19] When such structural changes are repeated, anisotropic volume changes accumulate, and since the variation along the *c*-axis is greater than that along the *a*-axis, directional stress builds up inside the particles (Fig. S23). The NCM80 composite cathode, similar to NMX75, showed stable interfaces between CAMs and SEs without void formation before cycling (Fig. S24). Under a higher pressure condition of 200 MPa during cycling, the measured pressure change in the NCM80 composite cathode was confirmed to be larger than that of the NMX75 composite cathodes (Fig. S25). As a result, loss of contact between the CAM and the SE occurs, leading to reduced ionic and electronic conductivity and promoting interfacial side reactions, which ultimately degrade the overall battery performance. XPS analysis revealed that NCM80 composite cathode exhibited more pronounced decomposition of LPSC compared to NMX75 composite cathode after 10 cycles (Fig. S26). Fig. 5c presents the calculated energy densities of full-cells employing NMX75 and NCM80 composite cathode using Li metal anode in ASSBs. At cut-off voltages of 4.25 V and 4.45 V, the energy densities for full-cell employing NMX75 composite cathodes were 546.5 Wh kg^{-1} and 701.6 Wh kg^{-1}, respectively, while those for full-cell employing NCM80 composite cathodes were 595.0 Wh kg^{-1} and 675.1 Wh kg^{-1}. The full-cell employing NMX75 composite cathode exhibits a higher energy density under high-voltage operation compared to the full-cell employing NCM60 composite cathodes (Table S4). These results indicate that the Co-free NMX material is eligible for commercialization as a high-energy-density cathode for next-generation ASSBs under high-voltage conditions.

Conclusion

In this study, we investigated the electrochemical performance and interfacial stability of a single-crystalline Co-free layered oxide cathode, NMX75, in sulfide-based ASSBs. Compared to conventional Co-containing cathodes such as NCM60 and NCM80, NMX75 demonstrated superior cycling stability and rate capability, particularly under high-voltage operation (up to 4.45 V). This enhanced performance is attributed to the electrochemo-mechanical properties of NMX75, including lower anisotropic volume change, improved lattice stability upon deep delithiation, and better preservation of solid–solid interfacial contact. EIS and DRT analysis further revealed sup-

pressed interfacial resistance growth during cycling. Structural and interfacial analyses using FIB-SEM, *ex situ* XRD, STEM-EDS, XPS, and ToF-SIMS confirmed that NMX75 undergoes less element interdiffusion and forms fewer interfacial decomposition products compared to NCM materials. Overall, this work highlights NMX75 as a promising Co-free cathode material for next-generation high-energy ASSBs, offering improved electrochemical performance and interfacial stability enabled by superior electrochemo-mechanical integrity.

Experimental section

Fabrication of cathode electrode

The cathode electrode was fabricated *via* a dry-film process. Li $[Ni_{0.75}Mn_{0.25}]O_2$ (NMX75, LG Chem Ltd) and Li_6PS_5Cl solid electrolyte (LPSC SE, D50 = 3 μm, CIS) were first mixed in a weight ratio of 75 : 22 with a mortar. After 20 minutes of initial mixing, carbon nanofiber (CNF, Sigma-Aldrich) and PTFE powder were added and further mixed for 20 minutes. Finally, the cathode dry-film was prepared in a weight ratio of 75 : 22 : 2 : 1 (active material : SE : CNF : PTFE). Li $[Ni_{0.60}Mn_{0.20}Co_{0.20}]O_2$ (NCM60, LG Chem Ltd) and Li $[Ni_{0.80}Co_{0.10}Mn_{0.10}]O_2$ (NCM80, Alfa Aesar) dry-films were also fabricated using the same procedure.

Characterization of materials

The X-ray photoelectron spectroscopy (XPS, K-alpha plus, ThermoFisher Scientific) and X-ray diffraction (XRD, D8 ADVANCE, Bruker) were used to analyze the elemental composition and crystallinity of the cathode active material before and after charging. All XPS spectra were calibrated by referencing the C 1s peak at 284.4 eV, corresponding to non-oxidized carbon. The reaction products generated before and after charging were identified by time-of-flight secondary ion mass spectrometry (TOF-SIMS, ION-TOF GmbH, Münster) using a 30 keV Bi_1primary ion beam at a current of 1.0 pA. The decomposition layers on the surfaces of the solid electrolyte (SE) and cathode active material (CAM) were investigated using high-resolution transmission electron microscopy (HR-TEM, NEO ARM, JEOL). TEM samples were prepared from the dry-film electrodes using focused ion beam (FIB, Scios, ThermoFisher Scientific). The electrode microstructures were examined using field-emission scanning electron microscopy (FE-SEM, JSM-7600F, JEOL).

Electrochemical evaluation

To fabricate all-solid-state battery (ASSB) cells, a tri-layer pellet (cathode dry-film|SE|Li) composed of a cathode dry-film, solid electrolyte (SE), and lithium metal was assembled. Initially, 35 mg of the pressed cathode dry-film and 150 mg of Li_6PS_5Cl powder were loaded into a polycarbonate tube (13 mm in diameter) and compressed under 420 MPa. Subsequently, a lithium metal foil (200 μm thick) was placed on the SE layer and pressed at 70 MPa. All ASSB cells were assembled in an Ar-filled glovebox.

Electrochemical performance was evaluated using a battery tester (TOSCAT 3000, Toyo Systems) at 25 °C, with cut-off voltage ranges of 2.5–4.25 V and 2.5–4.45 V under an external pressure of 20 MPa. In the cycling performance test, the first charge was conducted at 0.1C in constant-current constant-voltage (CC–CV) mode with a limiting current of 0.05C, and discharged at 0.1C. Subsequent cycles were charged at 0.2C using the same CC–CV mode and limiting current, and discharged at 0.2C. During rate capability testing, the charge rate was maintained at 0.1C using the CC–CV protocol, with a cutoff current set to 0.05C.

Electrochemical impedance spectroscopy (EIS) was performed using a potentiostat (ZIVE BP2, WonATech) over a frequency range of 0.01 Hz to 1 MHz with a 20 mV amplitude. Distribution of relaxation time (DRT) analysis was carried out using a MATLAB-based program developed by T. H. Wan *et al.* The galvanostatic intermittent titration technique (GITT) was performed by applying a 0.1C pulse current for 10 minutes, followed by a 2-hour relaxation period, from which the Li ion mobility was calculated.

The change in cell thickness of NMX75|SE|LTO, NCM60|SE|LTO, and NCM80|SE|LTO cells under varying pressures were measured using a digital electric press (TPU-040, TERALEADER Co., Ltd).

Author contributions

J. J. and J. P. conceived the concept and analyzed the results. U. P. and T. S. supervised the project. J. J. and J. P. designed the experiments and wrote the manuscript with assistance from J. K. and S. L. J. L., J. J., and Y. L. carried out materials characterization and electrochemical measurements. B. C. and S. Y. prepared the samples. J. J. and J. S. performed TOF-SIMS measurements. All authors reviewed and commented on the manuscript.

Conflicts of interest

There are no conflicts to declare.

Data availability

The data supporting this article have been included as part of the SI.

Supplementary Information is available, including particle size distributions, XRD, TEM, SEM, XPS, ToF-SIMS, cycling performance, voltage profiles, EIS, and ICP data. See DOI: https://doi.org/10.1039/d5eb00136f.

Acknowledgements

This work was supported by Korea Institute for Advancement of Technology (KIAT) grant funded by the Korea Government (MOTIE) (RS-2024-00417730, HRD Program for Industrial Innovation). This work was also supported by "Human

Resources Program in Energy Technology" of the Korea Institute of Energy Technology Evaluation and Planning (KETEP), granted financial resources from the Ministry of Trade, Industry & Energy, Republic of Korea (No. 20214000000520).

References

1 J. D. Sachs, *Lancet*, 2012, **379**, 2206–2211.
2 X. Wu, B. Fu, S. Wang, S. Song, Y. Li, Z. Xu, Y. Wei and J. Liu, *Nat. Sustain.*, 2022, **5**, 452–459.
3 M. Baumann, J. Peters, M. Weil and A. Grunwald, *Energy Technol.*, 2017, **5**, 1071–1083.
4 D. Lee, H. Lee, T. Song and U. Paik, *Adv. Energy Mater.*, 2022, **12**, 2200948.
5 P. Jaumaux, J. Wu, D. Shanmukaraj, Y. Wang, D. Zhou, B. Sun, F. Kang, B. Li, M. Armand and G. Wang, *Adv. Funct. Mater.*, 2021, **31**, 2008644.
6 J. Janek and W. G. Zeier, *Nat. Energy*, 2016, **1**, 1–4.
7 Y. Tian, G. Zeng, A. Rutt, T. Shi, H. Kim, J. Wang, J. Koettgen, Y. Sun, B. Ouyang and T. Chen, *Chem. Rev.*, 2020, **121**, 1623–1669.
8 D. H. Tan, E. A. Wu, H. Nguyen, Z. Chen, M. A. Marple, J.-M. Doux, X. Wang, H. Yang, A. Banerjee and Y. S. Meng, *ACS Energy Lett.*, 2019, **4**, 2418–2427.
9 P. Adeli, J. D. Bazak, K. H. Park, I. Kochetkov, A. Huq, G. R. Goward and L. F. Nazar, *Angew. Chem., Int. Ed.*, 2019, **58**, 8681–8686.
10 T. Schmaltz, F. Hartmann, T. Wicke, L. Weymann, C. Neef and J. Janek, *Adv. Energy Mater.*, 2023, **13**, 2301886.
11 L. de Biasi, B. Schwarz, T. Brezesinski, P. Hartmann, J. Janek and H. Ehrenberg, *Adv. Mater.*, 2019, **31**, 1900985.
12 J. Kim, M. J. Kim, J. Kim, J. W. Lee, J. Park, S. E. Wang, S. Lee, Y. C. Kang, U. Paik and D. S. Jung, *Adv. Funct. Mater.*, 2023, **33**, 2211355.
13 F. Walther, F. Strauss, X. Wu, B. Mogwitz, J. Hertle, J. Sann, M. Rohnke, T. Brezesinski and J. r. Janek, *Chem. Mater.*, 2021, **33**, 2110–2125.
14 J. Kim, S. Lee, H. Lee, J. Park, J. Lee, J. Park, J. Kim, J. Kwon, J. Jin and J. Cho, *eTransportation*, 2024, **19**, 100306.
15 S.-M. Bak, E. Hu, Y. Zhou, X. Yu, S. D. Senanayake, S.-J. Cho, K.-B. Kim, K. Y. Chung, X.-Q. Yang and K.-W. Nam, *ACS Appl. Mater. Interfaces*, 2014, **6**, 22594–22601.
16 R. Zhang, C. Wang, P. Zou, R. Lin, L. Ma, L. Yin, T. Li, W. Xu, H. Jia and Q. Li, *Nature*, 2022, **610**, 67–73.
17 J. U. Choi, N. Voronina, Y. K. Sun and S. T. Myung, *Adv. Energy Mater.*, 2020, **10**, 2002027.
18 J. L. Shi, D. D. Xiao, M. Ge, X. Yu, Y. Chu, X. Huang, X. D. Zhang, Y. X. Yin, X. Q. Yang and Y. G. Guo, *Adv. Mater.*, 2018, **30**, 1705575.
19 L. de Biasi, A. O. Kondrakov, H. Geßwein, T. Brezesinski, P. Hartmann and J. Janek, *J. Phys. Chem. C*, 2017, **121**, 26163–26171.
20 R. Koerver, I. Aygün, T. Leichtweiß, C. Dietrich, W. Zhang, J. O. Binder, P. Hartmann, W. G. Zeier and J. r. Janek, *Chem. Mater.*, 2017, **29**, 5574–5582.
21 C. Wang, J. T. Kim, C. Wang and X. Sun, *Adv. Mater.*, 2023, **35**, 2209074.
22 Y. Liang, H. Liu, G. Wang, C. Wang, Y. Ni, C. W. Nan and L. Z. Fan, *InfoMat*, 2022, **4**, e12292.
23 L. Li, H. Duan, J. Li, L. Zhang, Y. Deng and G. Chen, *Adv. Energy Mater.*, 2021, **11**, 2003154.
24 S. Ohno, R. Koerver, G. Dewald, C. Rosenbach, P. Titscher, D. Steckermeier, A. Kwade, J. r. Janek and W. G. Zeier, *Chem. Mater.*, 2019, **31**, 2930–2940.
25 A. Banerjee, X. Wang, C. Fang, E. A. Wu and Y. S. Meng, *Chem. Rev.*, 2020, **120**, 6878–6933.
26 Z. Wu, X. Li, C. Zheng, Z. Fan, W. Zhang, H. Huang, Y. Gan, Y. Xia, X. He and X. Tao, *Electrochem. Energy Rev.*, 2023, **6**, 10.
27 J. Haruyama, K. Sodeyama and Y. Tateyama, *ACS Appl. Mater. Interfaces*, 2017, **9**, 286–292.
28 A. O. Kondrakov, A. Schmidt, J. Xu, H. Geßwein, R. Mönig, P. Hartmann, H. Sommer, T. Brezesinski and J. r. Janek, *J. Phys. Chem. C*, 2017, **121**, 3286–3294.
29 F. Strauss, L. de Biasi, A.-Y. Kim, J. Hertle, S. Schweidler, J. r. Janek, P. Hartmann and T. Brezesinski, *ACS Mater. Lett.*, 2019, **2**, 84–88.
30 R. Ruess, S. Schweidler, H. Hemmelmann, G. Conforto, A. Bielefeld, D. A. Weber, J. Sann, M. T. Elm and J. Janek, *J. Electrochem. Soc.*, 2020, **167**, 100532.
31 B. X. Shi, Y. Yusim, S. Sen, T. Demuth, R. Ruess, K. Volz, A. Henss and F. H. Richter, *Adv. Energy Mater.*, 2023, **13**, 2300310.
32 P. Minnmann, F. Strauss, A. Bielefeld, R. Ruess, P. Adelhelm, S. Burkhardt, S. L. Dreyer, E. Trevisanello, H. Ehrenberg and T. Brezesinski, *Adv. Energy Mater.*, 2022, **12**, 2201425.
33 C. Doerrer, I. Capone, S. Narayanan, J. Liu, C. R. Grovenor, M. Pasta and P. S. Grant, *ACS Appl. Mater. Interfaces*, 2021, **13**, 37809–37815.
34 H. Zhang, X. He, Z. Chen, Y. Yang, H. Xu, L. Wang and X. He, *Adv. Energy Mater.*, 2022, **12**, 2202022.
35 S. Payandeh, C. Njel, A. Mazilkin, J. H. Teo, Y. Ma, R. Zhang, A. Kondrakov, M. Bianchini and T. Brezesinski, *Adv. Mater. Interfaces*, 2023, **10**, 2201806.
36 E. Trevisanello, R. Ruess, G. Conforto, F. H. Richter and J. Janek, *Adv. Energy Mater.*, 2021, **11**, 2003400.
37 F. Zhang, S. Lou, S. Li, Z. Yu, Q. Liu, A. Dai, C. Cao, M. F. Toney, M. Ge and X. Xiao, *Nat. Commun.*, 2020, **11**, 3050.
38 X. Fan, Y. Liu, X. Ou, J. Zhang, B. Zhang, D. Wang and G. Hu, *Chem. Eng. J.*, 2020, **393**, 124709.
39 H. Jeon, D.-H. Kwon, H. Kim, J.-H. Lee, Y. Jun, J.-W. Son and S. Park, *Chem. Eng. J.*, 2022, **445**, 136828.
40 H.-H. Ryu, B. Namkoong, J.-H. Kim, I. Belharouak, C. S. Yoon and Y.-K. Sun, *ACS Energy Lett.*, 2021, **6**, 2726–2734.
41 A. Aishova, G. T. Park, C. S. Yoon and Y. K. Sun, *Adv. Energy Mater.*, 2020, **10**, 1903179.

42 Y.-h. Luo, H.-x. Wei, L.-b. Tang, Y.-d. Huang, Z.-y. Wang, Z.-j. He, C. Yan, J. Mao, K. Dai and J.-c. Zheng, *Energy Storage Mater.*, 2022, **50**, 274–307.
43 T. Liu, L. Yu, J. Liu, J. Lu, X. Bi, A. Dai, M. Li, M. Li, Z. Hu and L. Ma, *Nat. Energy*, 2021, **6**, 277–286.
44 J. Shen, B. Zhang, W. Huang, X. Li, Z. Xiao, J. Wang, T. Zhou, J. Wen, T. Liu and K. Amine, *Adv. Funct. Mater.*, 2023, **33**, 2300081.
45 J. Auvergniot, A. Cassel, J.-B. Ledeuil, V. Viallet, V. Seznec and R. Dedryvère, *Chem. Mater.*, 2017, **29**, 3883–3890.
46 F. Walther, R. Koerver, T. Fuchs, S. Ohno, J. Sann, M. Rohnke, W. G. Zeier and J. r. Janek, *Chem. Mater.*, 2019, **31**, 3745–3755.
47 S. K. Jung, H. Kim, S. H. Song, S. Lee, J. Kim and K. Kang, *Adv. Funct. Mater.*, 2022, **32**, 2108790.
48 Y.-K. Sun, D.-J. Lee, Y. J. Lee, Z. Chen and S.-T. Myung, *ACS Appl. Mater. Interfaces*, 2013, **5**, 11434–11440.
49 J. Zheng, W. H. Kan and A. Manthiram, *ACS Appl. Mater. Interfaces*, 2015, **7**, 6926–6934.
50 S. Hori, R. Kanno, X. Sun, S. Song, M. Hirayama, B. Hauck, M. Dippon, S. Dierickx and E. Ivers-Tiffée, *J. Power Sources*, 2023, **556**, 232450.
51 F. Strauss, T. Bartsch, L. de Biasi, A.-Y. Kim, J. r. Janek, P. Hartmann and T. Brezesinski, *ACS Energy Lett.*, 2018, **3**, 992–996.
52 J.-C. Dupin, D. Gonbeau, H. Benqlilou-Moudden, P. Vinatier and A. Levasseur, *Thin Solid Films*, 2001, **384**, 23–32.
53 C. Kim, J. Kim, J. Park, J. Kim, S. Lee, S. Sun, S. Myung, D. Lee, K. Park and I. Jang, *Adv. Energy Mater.*, 2021, **11**, 2102045.
54 B. K. Park, H. Kim, K. S. Kim, H. S. Kim, S. H. Han, J. S. Yu, H. J. Hah, J. Moon, W. Cho and K. J. Kim, *Adv. Energy Mater.*, 2022, **12**, 2201208.
55 P. Vadhva, J. Hu, M. J. Johnson, R. Stocker, M. Braglia, D. J. Brett and A. J. Rettie, *ChemElectroChem*, 2021, **8**, 1930–1947.
56 L. Zhang, Y. Dai, C. Li, Y. Dang, R. Zheng, Z. Wang, Y. Wang, Y. Cui, H. Arandiyan and Z. Shao, *Energy Storage Mater.*, 2024, 103378.
57 Y. Morino and S. Kanada, *J. Power Sources*, 2021, **509**, 230376.
58 Y. Morino, H. Sano, S. Kawaguchi, S. Hori, A. Sakuda, T. Takahashi, N. Miyashita, A. Hayashi and R. Kanno, *J. Phys. Chem. C*, 2023, **127**, 18678–18683.
59 J. Illig, M. Ender, T. Chrobak, J. P. Schmidt, D. Klotz and E. Ivers-Tiffée, *J. Electrochem. Soc.*, 2012, **159**, A952.
60 R. He, Y. He, W. Xie, B. Guo and S. Yang, *Energy*, 2023, **263**, 125972.
61 J. W. Yap, T. Wang, H. Cho and J.-H. Kim, *Electrochim. Acta*, 2023, **446**, 142108.
62 C.-Y. Yu, J. Choi, J. Dunham, R. Ghahremani, K. Liu, P. Lindemann, Z. Garver, D. Barchiesi, R. Farahati and J.-H. Kim, *J. Power Sources*, 2024, **597**, 234116.
63 C. Wei, D. Yu, X. Xu, R. Wang, J. Li, J. Lin, S. Chen, L. Zhang and C. Yu, *Chem. – Asian J.*, 2023, **18**, e202300304.
64 B. Liu, S. D. Pu, C. Doerrer, D. Spencer Jolly, R. A. House, D. L. Melvin, P. Adamson, P. S. Grant, X. Gao and P. G. Bruce, *SusMat*, 2023, **3**, 721–728.
65 A. Sakuda, A. Hayashi and M. Tatsumisago, *Chem. Mater.*, 2010, **22**, 949–956.
66 R. A. House, U. Maitra, L. Jin, J. G. Lozano, J. W. Somerville, N. H. Rees, A. J. Naylor, L. C. Duda, F. Massel and A. V. Chadwick, *Chem. Mater.*, 2019, **31**, 3293–3300.
67 S. Wenzel, S. J. Sedlmaier, C. Dietrich, W. G. Zeier and J. Janek, *Solid State Ionics*, 2018, **318**, 102–112.